# Photocurrent Spectroscopy of Perovskite Solar Cells Over a Wide Temperature Range from 15 K to 350 K

*Jay B. Patel, Qianqian Lin, Olga Zadvorna, Christopher L. Davies, Laura M. Herz, Michael B. Johnston**

Department of Physics, Clarendon Laboratory, University of Oxford, Parks Road, Oxford, OX1 3PU, UK

Email: michael.johnston@physics.ox.ac.uk

# Supporting Information

**Contents**

## Experimental Techniques

### *Device Fabrication*

The devices were fabricated as reported previously.[1] Briefly, the Fluorine doped Tin Oxide (FTO) coated glass substrates (Tec 15 Pilkington) were cleaned thoroughly. The substrates were placed in a $TiCl_4$ bath, to create a thin layer of $TiO_2$. Thereafter PCBM (7.5mg/ml) dissolved in DCB was spincoated on the FTO substrate.

For the $MAPbI_3$ based devices; $MAPbI_3$ films were deposited using the dual source thermal evaporation method.[1]

For the $PbI_2$ based device; Lead(II) iodide, ultra-dry 99.999% (metals basis) was evaporated at $0.4As^{-1}$ at $2x10^{-6}$ mbar.

The films were not annealed. Spiro-OMeTAD was then deposited via the spin coating method. Finally, 100nm silver electrodes were deposited by thermal evaporation.

### *Photocurrent Spectroscopy*

Photocurrent was measured via a custom-built Fourier transform photocurrent spectrometer based on a Bruker Vertex 80v Fourier Transform Interferometer. Devices were illuminated with a tungsten halogen light source. The solar cells were masked with a metal aperture, with a defined active area, 0.0625 $cm^2$. A current preamplifier, Stanford Research 570, was used to detect low currents. For the temperature-dependent measurements, the solar cell was placed on a copper cold finger, that included two sensors, one at the tip and one in the middle. This allowed for accurate recording of the temperature. All the photocurrent measurements were carried out in vacuum.

### *Device Characterization*

Device current-voltage characteristics were measured under simulated AM1.5, 100 mW $cm^{-2}$ sunlight (1 sun), ABET Technologies Sun 2000, and a Keithly 2400 Sourcemeter in ambient conditions.

For the in-situ current-voltage characterization, during the photocurrent experiment, the light source used was a tungsten halogen lamp. A Keithly 2450 source meter was used to measure both the current and voltage.

***UV-Vis absorption spectroscopy***

Transmission and reflection measurements were taken using a Bruker Vertex 80v Fourier Transform Interferometer with a silicon diode detector and a tungsten halogen light as a near infrared source. A xenon lamp was used as a UV light source. Temperature-dependent measurement were carried out in a gas exchange helium cryostat.

***Scanning Electron Microscopy***

Images were taken using a Hitachi S-4300 microscope using 3kV accelerating voltage. The substrates were coated with 3nm of Platinum.

***Spectrally Calibrated Photocurrent Spectra***

Photocurrent Spectra was spectrally calibrated by dividing the photocurrent spectrum of the $MAPbI_3$ device with a calibrated reference silicon diode

***Internal Quantum Efficiency***

The internal quantum efficiency (IQE) (Figure 3d) was calculated by dividing the external quantum efficiency spectrum (EQE) (Figure S8) by the percentage of absorbed photons (extracted directly from the absorption data shown Figure S5). The EQE spectra were calibrated using a certified Newport reference silicon solar cell.

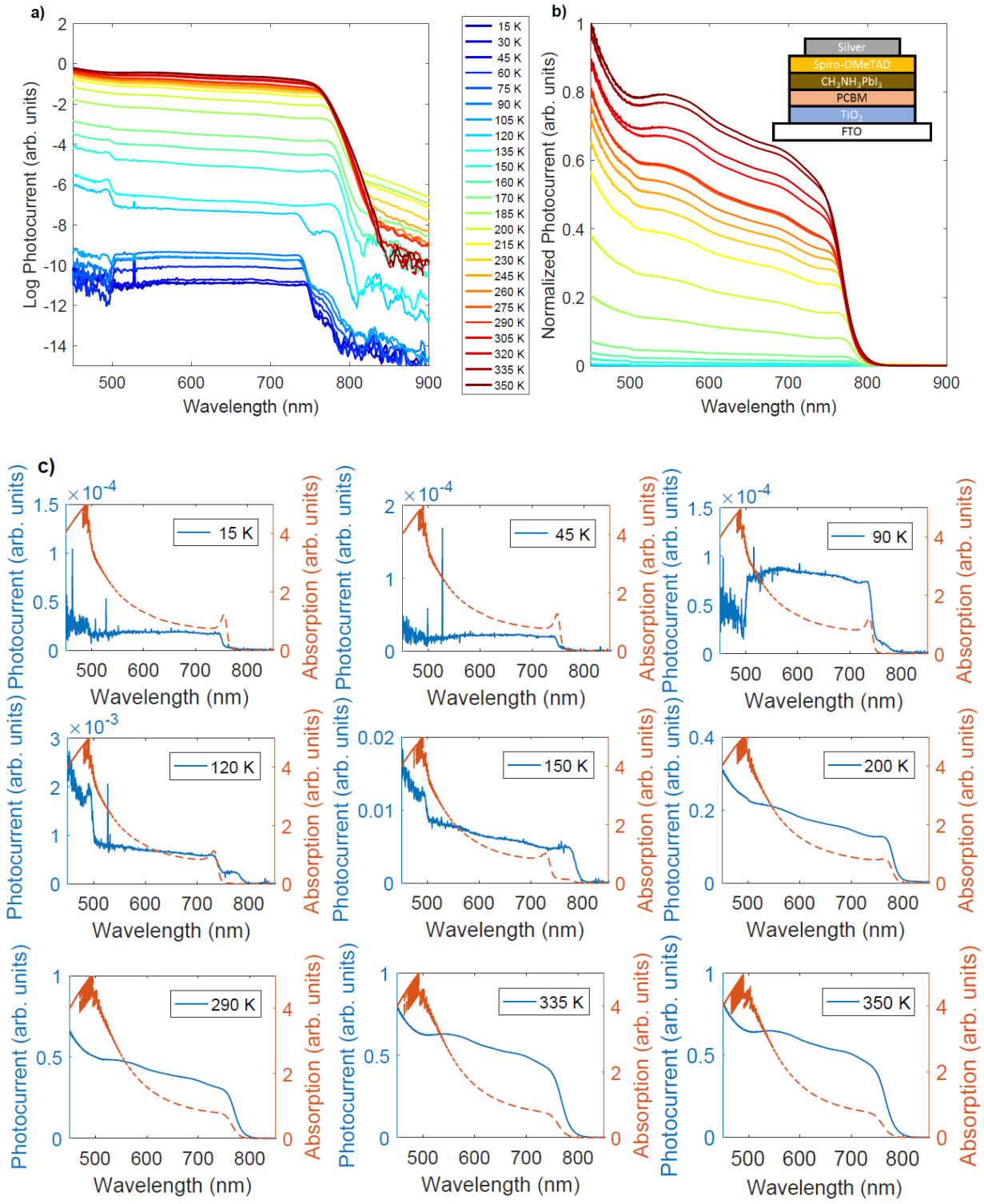


**Figure S1 a)** Full temperature dependence of photocurrent data from the device presented in Figures 1-4 in the main manuscript. **b)** Photocurrent normalized with respect to the photocurrent spectra of the $MAPbI_3$ device taken at 350K, the inset shows the $MAPbI_3$ device architecture used. **c)** Raw photocurrent spectra taken at the shown temperatures (blue solid line), with the corresponding absorption spectra of the device at that temperature (red dashed line).

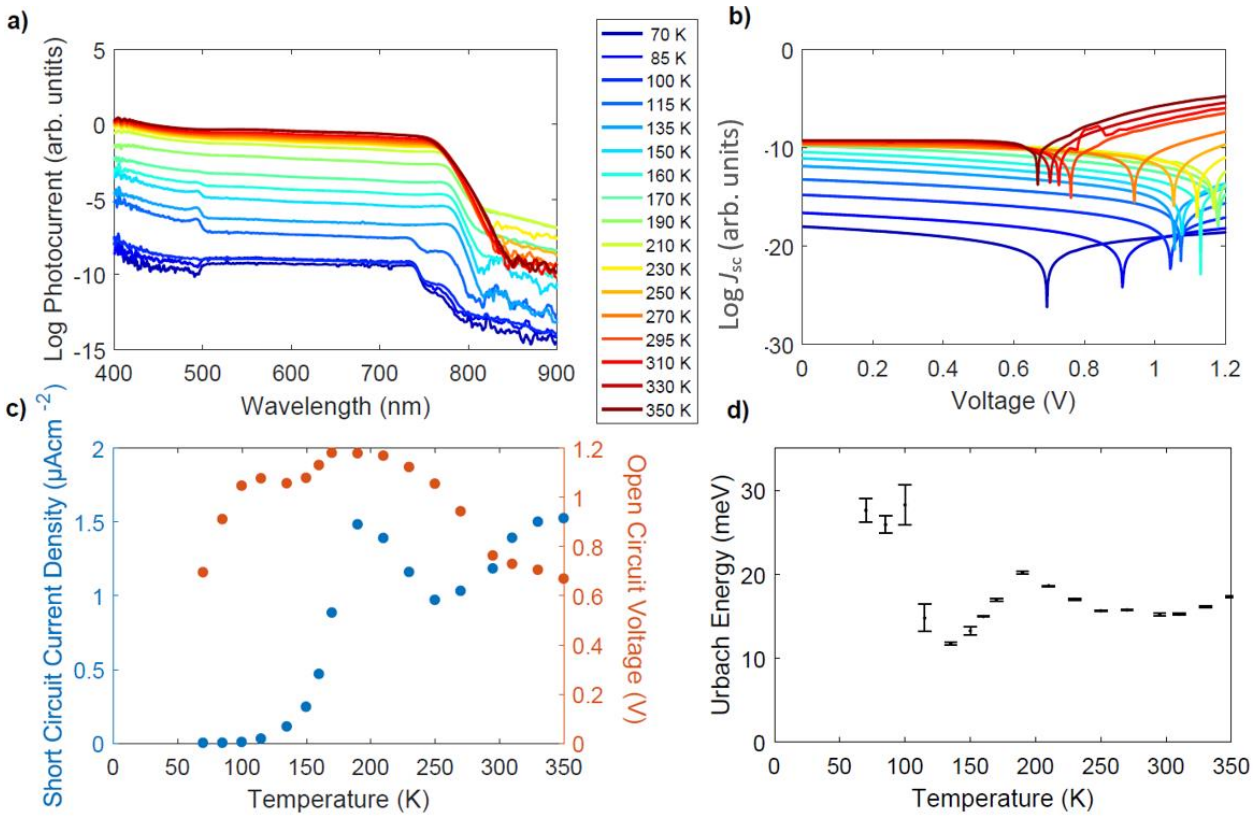


**Figure S2 a)** Temperature-dependent photocurrent spectra for another device (device 2) with the same architecture as shown in Figure 1 and S1. The results confirm the observation of the $PbI_2$ photocurrent contribution, and the coexistence of the orthorhombic and tetragonal phases at low temperatures in $MAPbI_3$ devices. **b)** Temperature-dependent current-voltage curves plotted on a semi-log scale. **c)** Short circuit current density and open circuit voltage of the device as a function of temperature, when illuminated by the tungsten lamp. Interestingly the voltage peaks between 190 K and 210 K. **d)** Temperature dependence of the Urbach energy. The error bars for data points below the 115 K are large, owing to the coexistence of two phases, the tetragonal and orthorhombic within the $MAPbI_3$ film.

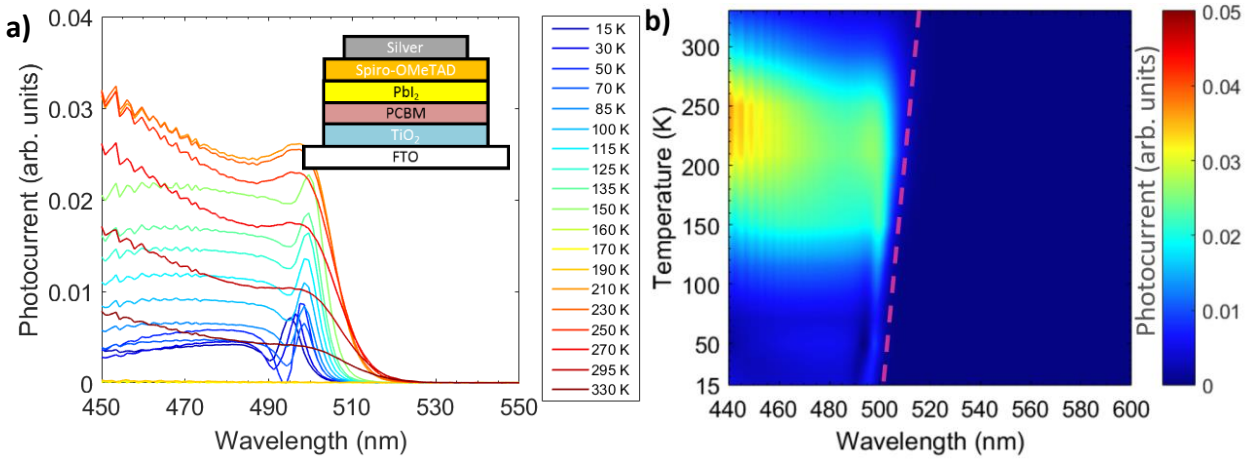


**Figure S3 a)** The photocurrent spectra for a device with $PbI_2$ as the absorber material in the device. The inset shows the $PbI_2$ device architecture used in this experiment. **b)** Colormap of the $PbI_2$ device photocurrent spectra. The colormap clearly shows the red shift of the photocurrent onset (purple line) at increasing temperatures, as observed in absorption measurements.[2,3]

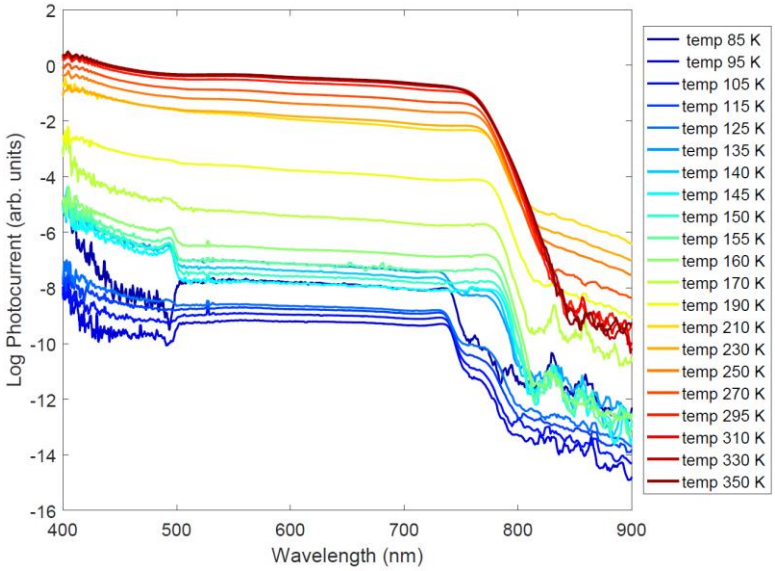


**Figure S4)** Temperature-dependent photocurrent spectra for another $MAPbI_3$ device (device 3) with the same architecture as shown in Figure 1. This figure reiterates the observation of the $PbI_2$ photocurrent contribution, and the coexistence of the orthorhombic and tetragonal phases at low temperatures.

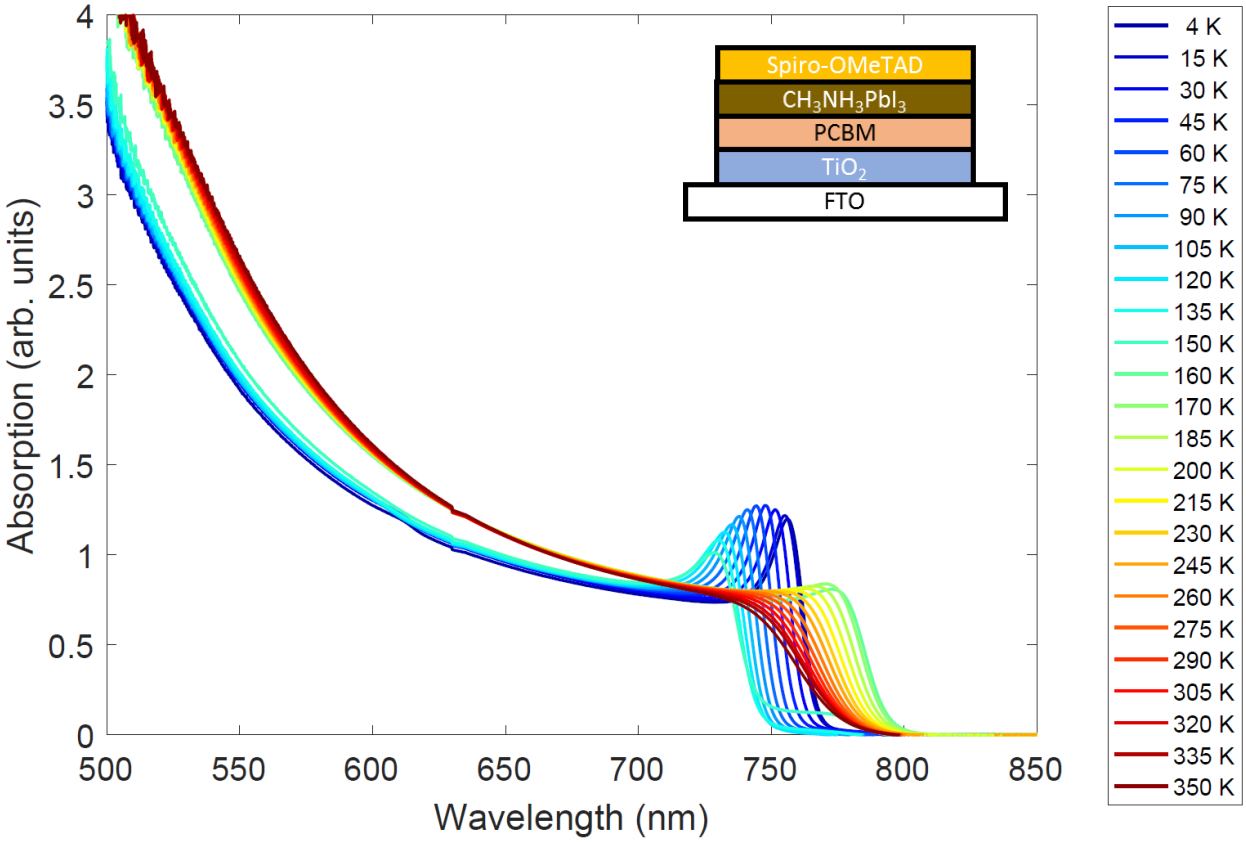


**Figure S5)** Temperature-dependent absorption spectra of the device whose architecture is shown in the inset. The device used was from the same batch of the devices tested for the photocurrent experiments, albeit with the silver electrodes removed.

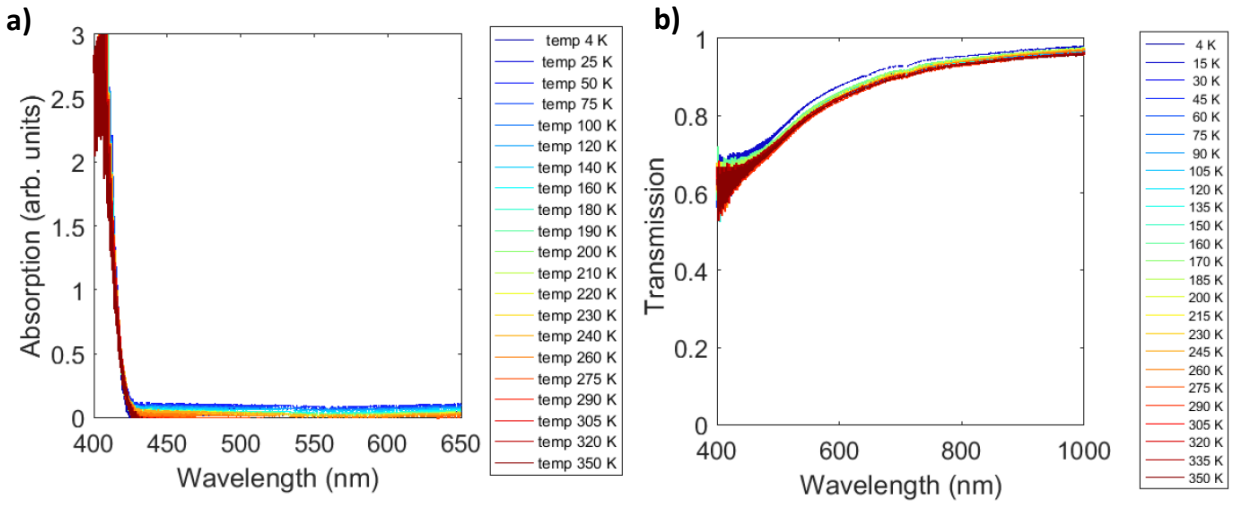


**Figure S6 a)** Temperature-dependent absorption of a thin film of Spiro-OMeTAD. **b)** Temperature-dependent transmission of a thin film of PCBM.

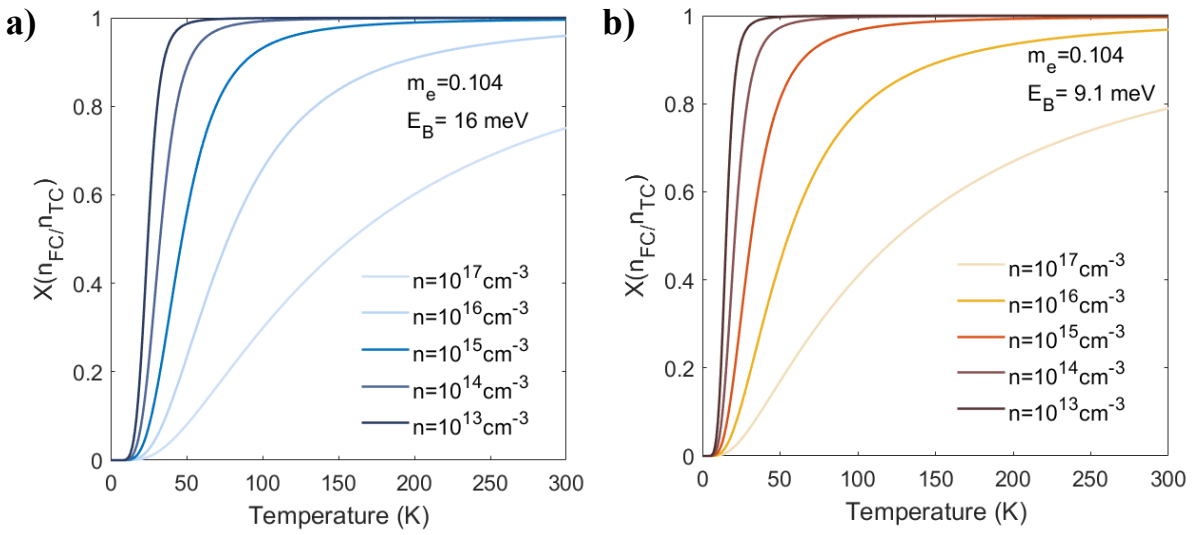


**Figure S7)** Simulation of the free charge fraction (X) over the total excitation density (n). The model is based on the method presented in Ref. 4. The total excitation density at AM1.5, 1 sun is between $10^{13}$ and $10^{15}$ $cm^{-3}$ (ref. 4). The reduced mass of the exciton is 0.104 $m_e$ (ref. 5) and the exciton binding energy is **a)** based on magneto-optical experiments (ref. 5) **b)** calculated from the spectra shown in Figure 4 and method used in figure S9.

The equation used is

$$\frac{x^2}{1-x} = \frac{1}{n}\left(\frac{2\pi\mu k_B T}{h^2}\right)^{\frac{3}{2}} e^{-\frac{E_B}{k_B T}} \qquad (1)$$

Where $E_B$ is the exciton binding energy, $k_B$ is the Boltzmann constant, $T$ is the temperature, $\mu$ is the effective mass of the exciton, $h$ is the Plank's constant, $n$ is the total excitation density and $x$ is the fraction of free charge carriers over the total density of excitation.

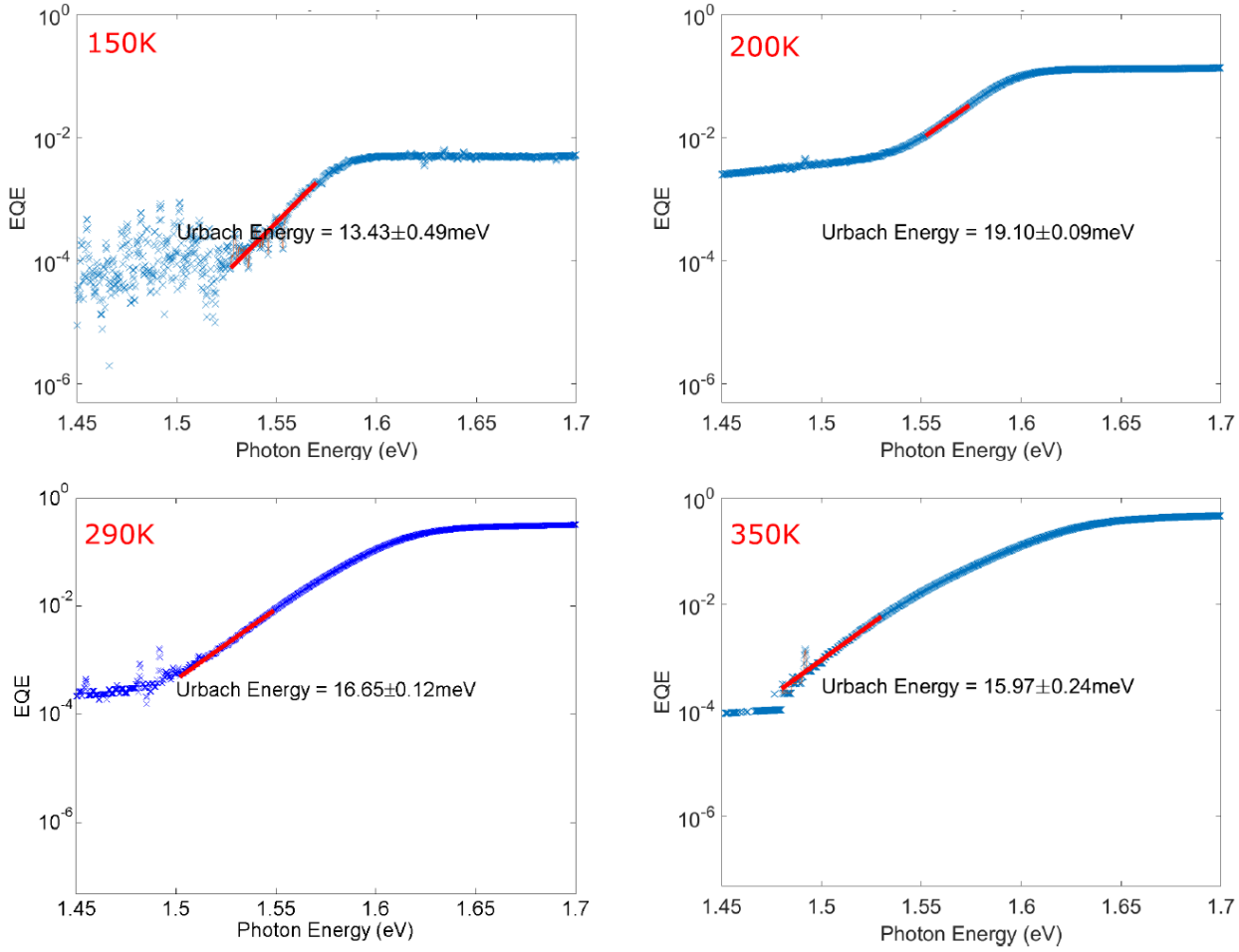


**Figure S8)** Urbach energy fits of the external quantum efficiency (EQE) of the device presented in Figure 2 in the manuscript. The Urbach energy was determined from the EQE which was obtained by processing the photocurrent data and using a calibrated silicon solar cell with a known EQE as a reference. A non-linear regression was performed using MATLAB to extract the Urbach energy from the EQE data. Robust fitting was performed using a bisquared (Tukey's biweight) weighting function. We calculated a 95% confidence interval for the Urbach energy using the residuals and Jacobian of the fit.

$$\eta = \eta_0 \, e^{\frac{h\nu - E_0}{E_U}} \qquad (2)$$

Equation 2 shows the determination of the Urbach energy from the tail of the band edge determined by the EQE. Where $\eta$ is the EQE, $h\nu$ is the photon energy and $E_U$ is the Urbach energy. $\eta_0$ and $E_0$ are constants.

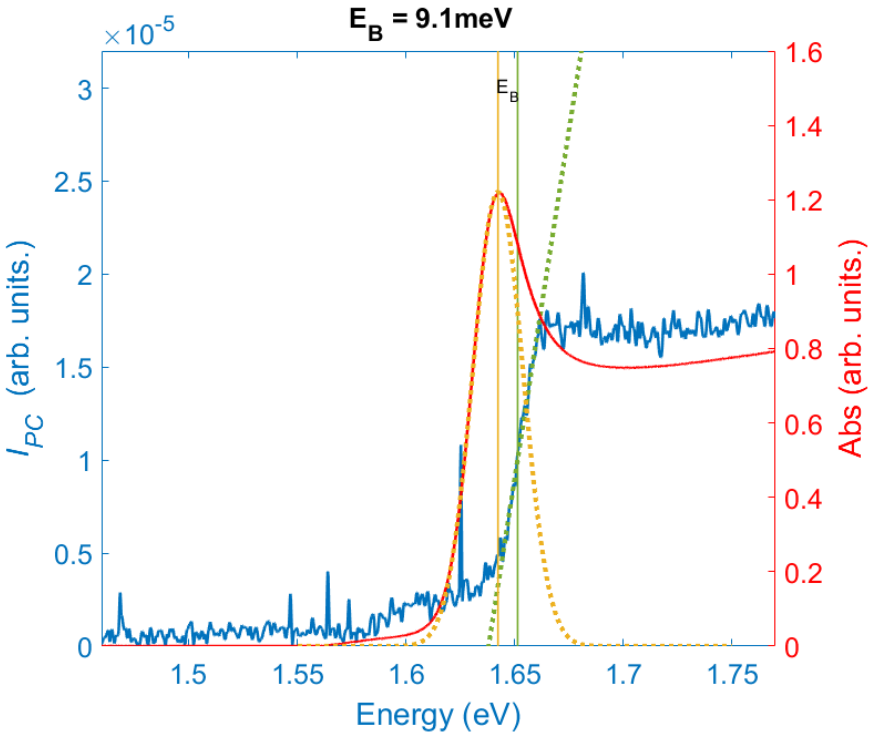


**Figure S9)** Photocurrent and absorption spectra of a $MAPbI_3$ device as depicted in Figure 4. A simple estimate of the lower bound of the exciton binding energy ($E_B$) was determined by the difference between midpoint of the photocurrent onset and the peak of the exciton in the absorption onset. The exciton was fitted with a Gaussian function using MATLAB. At 15 K, low thermal energy and zero applied bias ensure that most excitons will not dissociate (see figure S7) and hence will not contribute to the photocurrent. Therefore, the photocurrent onset represents the onset of the continuum states in the perovskite semiconductor.

**Table S1)** Average reverse scan device current-voltage characteristics of 7 devices from the batch used in this study. The champion device current-voltage characteristics are shown in Figure 1.

| | |
|---|---|
| **Average PCE (%)** | **12.19** |
| Standard Deviation | *1.32* |
| **Average $V_{oc}$ (V)** | **1.07** |
| Standard Deviation | *0.01* |
| **Average $J_{sc}$ (mAcm$^{-2}$)** | **17.59** |
| Standard Deviation | *0.94* |
| **Average FF** | **0.65** |
| Standard Deviation | *0.04* |

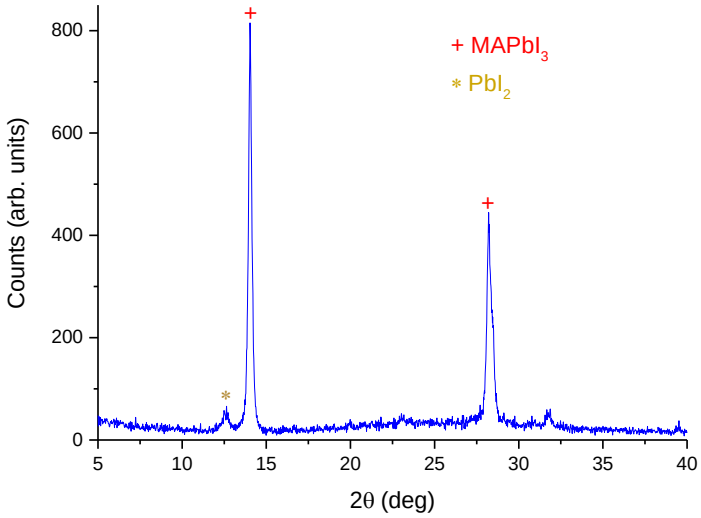


**Figure S10)** X-ray diffraction pattern for a vapor deposited perovskite thin film on glass. The parameters used for the growth of this film are identical to those used for the devices.

## References


(1) Patel, J. B.; Wong-Leung, J.; Van Reenen, S.; Sakai, N.; Wang, J. T. W.; Parrott, E. S.; Liu, M.; Snaith, H. J.; Herz, L. M.; Johnston, M. B. Influence of Interface Morphology on Hysteresis in Vapor-Deposited Perovskite Solar Cells. *Adv. Electron. Mater.* **2017**, *3*, 1600470.

(2) Ahuja, R.; Arwin, H.; Ferreira da Silva, A.; Persson, C.; Osorio-Guillén, J. M.; Souza de Almeida, J.; Moyses Araujo, C.; Veje, E.; Veissid, N.; An, C. Y.; et al. Electronic and Optical Properties of Lead Iodide. *J. Appl. Phys.* **2002**, *92*, 7219–7224.

(3) Gobinathan, R.; Hariharan, K.; Ramasamy, P. Electronic Absorption Spectra of Lead Iodide. *Krist. und Tech.* **1981**, *16*, 1435–1438.

(4) D'Innocenzo, V.; Grancini, G.; Alcocer, M. J. P.; Kandada, A. R. S.; Stranks, S. D.; Lee, M. M.; Lanzani, G.; Snaith, H. J.; Petrozza, A. Excitons versus Free Charges in Organo-Lead Tri-Halide Perovskites. *Nat. Commun.* **2014**, *5*, 45214.

(5) Miyata, A.; Mitioglu, A.; Plochocka, P.; Portugall, O.; Wang, J. T.-W.; Stranks, S. D.; Snaith, H. J.; Nicholas, R. J. Direct Measurement of the Exciton Binding Energy and Effective Masses for Charge Carriers in Organic–inorganic Tri-Halide Perovskites. *Nat. Phys.* **2015**, *11*, 582–587.